Cavitation Onset In Counter-Rotating Vortices From Diverging Disks

De Oliveira Barra Costa, M.; Fiscaletti, D.; Lambrechts, M.; van Zanten, R.R.; Wellens, P.R.; van Terwisga, T.J.C.; Westerweel, J.

Citation (APA)
De Oliveira Barra Costa, M., Fiscaletti, D., Lambrechts, M., van Zanten, R. R., Wellens, P. R., van Terwisga, T. J. C., & Westerweel, J. (2024). Cavitation Onset In Counter-Rotating Vortices From Diverging Disks. In *Proceedings of the 21st International Symposium on the Application of Laser and Imaging Techniques to Fluid Mechanics* Article 124 LISBON Simposia. https://doi.org/10.55037/lxlaser.21st.124

Important note
To cite this publication, please use the final published version (if applicable).
Please check the document version above.

Cavitation onset in counter-rotating vortices from diverging disks

Mariana Costa,[1] Daniele Fiscaletti,[2] Mallaury Lambrechts,[2] Renée van Zanten,[1]
Peter Wellens,[2] Tom van Terwisga,[2] Jerry Westerweel[1]

1: Laboratory for Aero and Hydrodynamics, Delft University of Technology, Mekelweg 2, 2628 CD Delft, The Netherlands
2: Maritime and Transport Technology, Delft University of Technology, Mekelweg 2, 2628 CD Delft, The Netherlands
*Corresponding author: M.DeOliveiraBarraCosta@tudelft.nl

Keywords: cavitation, vortices, pressure reconstruction.

ABSTRACT

Cavitation occurs when the local pressure, induced by high local velocities, drops below the vapor pressure, leading to the formation of vapor bubbles. The subsequent collapse of these bubbles can cause noise, erosion, and vibrations. Recent studies show that cavitation is sensitive to water quality, i.e., the nuclei populations, the chemical composition of water, and the presence of particles. Motivated by investigating the effects of water quality on cavitation, experiments are performed in a dedicated experimental facility. This consists in two co-axial disks that are initially at rest and mutually in contact, in a tank filled with water. The fast diverging movement of the top disk with respect to the bottom one produces a jet flow inside the gap between the disks, which leads to the formation of two counter-rotating vortices. The local pressure drop induced by high flow velocities leads to a phase change. To characterize the phenomenon, two optical techniques are applied, i.e., shadowgraphy and particle image velocimetry (PIV). In performing PIV reconstruction, the sum of correlation enhances the spatial resolution of the velocity vector fields. The pressure field in the region where the vortices occur is obtained from velocity data. The water quality effects on cavitation are investigated by adding salt and using water with an abundance of nuclei inside the tank.

1. Introduction

Cavitation is a multiphase phenomenon that can appear in ship propellers, pumps, valves, and other mechanical components (Franc & Michel, 2005). It occurs when the local pressure decreases below a critical pressure, typically deemed as the vapour pressure. The local pressure drop induced by high flow velocities or accelerations leads to a phase change and, consequently, to the formation of vapour bubbles, which can evolve into stable cavities. When collapsing, these pockets of vapour emit noise, and can cause erosion and vibrations to the nearby surfaces. Recent studies show that cavitation is sensitive to water quality, e.g. Brandner et al. (2022), where for water quality we intend the concentration and spectral density of the background nuclei, the chemical

composition of water, and the presence of particles. Gaining a better understanding into inception and development of cavitation when varying the water quality is relevant to ship propellers (Khoo et al., 2021), the geometry and functionality of valves (Resch & Scheidl, 2014), and the lubrication of articulations (Kawchuk et al., 2015).

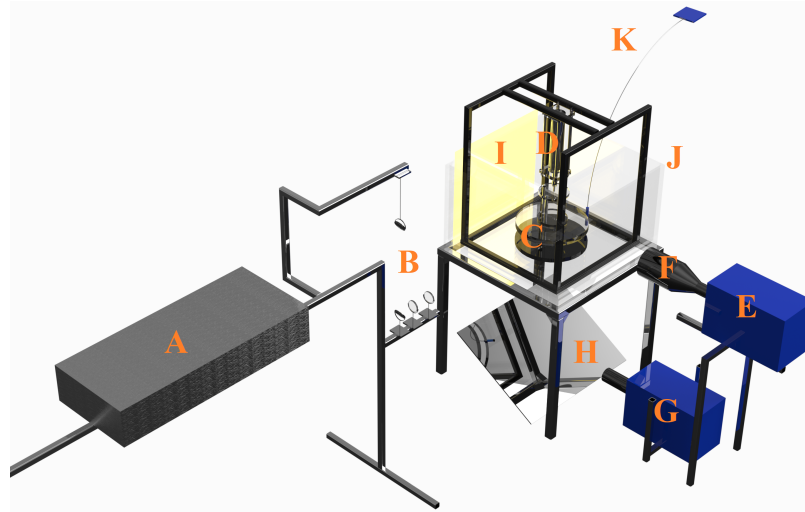## 2. Materials and methods

2.1. Experimental configuration

With the aim of investigating the effect of water quality on cavitation, a dedicated experimental facility is devised. This consists of two co-axial disks that are initially at rest, mutually at contact. Actuated by a pneumatic cylinder, the top disk moves vertically along the common axis, reaching maximum accelerations larger than 90 m s^{-2}. Two pressure values are set in the compressed-air system, i.e., 6 bar and 2 bar, which determine the two cases under investigation in this work, respectively Case 1 and Case 2. A thorough description of these two cases is reported in Table 1. The disks are placed in a 50×50×30 cm^3 tank filled with water. The flow developing in gap between the two disks which results from their rapid separation is known as the negative squeeze film, and it is particularly important in lubrication studies (Reynolds, 1886). The rapid diverging movement in combination with a small angle of the top disk with respect to the bottom one determines the formation of a non-uniform jet flow at the interface between the disks, which produces two counter-rotating vortices. The circulation around these vortices strengthens for increasing pressure in the compressed air system.

Table 1. Characterization of the two cases under study with respect to the maximum acceleration (a_{max}) and maximum velocity of the diverging disk (v_{max}), time to reach maximum acceleration (t_a) and maximum velocity (t_v), distance between the disks when the diverging disk reaches the maximum acceleration (d_a) and maximum velocity (d_v), and time between the disks when the diverging disk reaches its final position (t_p).

Case	a_{max} (m s^{-2})	v_{max} (m s^{-1})	t_a (ms)	t_v (ms)	d_a (mm)	d_v (mm)	t_p (ms)
1 (cavitating)	93	2	39	52	9.7	32.4	62.9
2 (non-cavitating)	28	1.1	117	140	10.2	32	162.1

Two techniques of flow investigation are applied in this research to unveil the physics of the phenomenon, i.e. shadowgraphy and particle image velocimetry (PIV). For the first technique, a LED panel is located behind the tank, providing parallel light rays that reach the sensor of one of the CMOS cameras. As for the PIV, a second camera records the displacement of the particle images. The water is seeded with fluorescent orange polyethylene microspheres having a diameter between 75 μm and 90 μm, which act as tracer particles. A dual-cavity laser creates a light sheet

perpendicular to the axes of the two disks. It is worth mentioning that an optical filter is positioned in front of the camera lens, transmitting mainly the light scattered by the fluorescent particles to the camera sensor, therefore increasing the signal-to-noise ratio of the measurements. A schematic showing the experimental setup is given in Figure 1.

Figure 1. Schematic of the experimental setup. A: laser; B: light-sheet optics; C: disks; D: pneumatic actuator; E: high-speed camera for shadowgraphy; F: telecentric lens; G: high-speed camera for PIV; H: mirror; I: LED panel; J: glass tank; K: oxygen meter.

The images are acquired using commercial software (Davis 10, LaVision GmbH). A code written in LabVIEW (National Instruments) enables the automatic triggering of the image acquisition and the movement of the top disk to occur in parallel. The displacement between the two disks, and, consequently, the velocity and acceleration, are estimated by imaging analysis of the shadowgraphy sequences on the vertical plane. A telecentric lens is used for shadowgraphy recordings because of its more precise measurement characteristics due to its low image distortion and field curvature (Konrath & Schröder, 2002; Erinin et al., 2023). Appropriately adjusting the lens position with respect to the horizontal axis is necessary to place the depth of focus exactly where the vortices are expected to appear. In relation to the PIV setup, a 105 mm focal length lens is used with a 2.8 f-number and 1:9 magnification. The laser sheet is positioned parallel to the disks, approximately 2.7 millimeters above the bottom disk. This has the aim of reconstructing the velocity vector field at the very beginning of the raising movement of the top disk, when the flow acceleration is the largest.

Ten repetitions for each value of the pressure of the pneumatic cylinder are performed, leading to a total of twenty acquisitions. According to Meinhart et al. (2000), correlation averaging, or sum of correlation, enables to increase the spatial resolution of the velocity fields. Hence, this post-processing technique is applied to the time-resolved correlation maps. In combination with PIV recordings, shadowgraphy images are also acquired simultaneously. This enables to select the PIV

image frames associated with the corresponding position of the upper disk in each repetition, to be used in the correlation averaging.

Double-frame PIV is later performed, and from applying correlation averaging as mentioned above, an interrogation window size of 8×8 px^2 is obtained, leading to a vector spacing of approximately 0.4×0.4 mm^2 for a 50% window overlapping. The appropriate time difference between the two frames for the two cases under analysis (see Table 1) is determined to be of 80 μs for Case 1, and 160 μs for Case 2. The acquisition rate in shadowgraphy is 1146 Hz when performed with PIV. When shadowgraphy solely is employed, the frame rate is 2289 Hz. The relation between pixels and mm is 10.28 pixels mm^{-1} for the PIV recordings, and 22.61 pixels mm^{-1} for the shadowgraphy images.

The dissolved oxygen content is measured using a PreSens FTM-PSt3 (with PT100) oxygen sensor. The measurements are given in percentages of air saturation units relative to atmospheric conditions, and are used as an approximation to the air dissolved in the water (Nanda et al., 2022). The assumption that the fraction of each gas in the mixture does not change is made to use this approximation.

2.2. Pressure reconstruction from PIV data

The pressure field is reconstructed from PIV data in the region where the vortices occur. The Navier-Stokes equations are firstly considered, written in the following form

$$\frac{\partial \mathbf{u}}{\partial t} + (\mathbf{u} \cdot \nabla)\mathbf{u} = -\frac{1}{\rho}\nabla p + \nu\nabla^2\mathbf{u} + \mathbf{f}, \tag{1}$$

where $\mathbf{u}$ is the velocity vector, p represents the pressure, ρ is the liquid density, ν is the kinematic viscosity and $\mathbf{f}$ is the body force.

By applying the identity $(\mathbf{u} \cdot \nabla)\mathbf{u} = \frac{1}{2}\nabla(\mathbf{u} \cdot \mathbf{u}) - \mathbf{u} \times \boldsymbol{\omega}$, where $\boldsymbol{\omega}$ is the vorticity, in Eq. (1), and rearranging the terms, we get

$$\frac{\partial \mathbf{u}}{\partial t} + \frac{1}{2}\nabla(\mathbf{u} \cdot \mathbf{u}) - \mathbf{u} \times \boldsymbol{\omega} = -\frac{1}{\rho}\nabla p + \nu\nabla^2\mathbf{u} + \mathbf{f}. \tag{2}$$

Considering that $k = \frac{1}{2}\mathbf{u} \cdot \mathbf{u} = \frac{1}{2}\mathbf{u}^2$ is the kinetic energy, P represents the pressure, p, divided by the liquid density ρ, disregarding body force $\mathbf{f}$ and taking the divergence of the Eq. (2) leads to

$$\nabla \cdot \frac{\partial \mathbf{u}}{\partial t} + \nabla^2 k - \nabla \cdot (\mathbf{u} \times \boldsymbol{\omega}) = -\nabla^2 P + \nabla \cdot (\nu\nabla^2\mathbf{u}). \tag{3}$$

If we consider the flow incompressible, $\nabla \cdot \frac{\partial \mathbf{u}}{\partial t} = \frac{\partial}{\partial t}(\nabla \cdot \mathbf{u}) = 0$, since $(\nabla \cdot \mathbf{u}) = 0$. Moreover, taking the identity $\nabla^2 \mathbf{u} = \nabla(\nabla \cdot \mathbf{u}) - \nabla \times (\nabla \times \mathbf{u})$ and knowing that the vorticity is the curl of the velocity vector, we obtain $\nabla^2 \mathbf{u} = -\nabla \times \boldsymbol{\omega}$. Since the divergence of a curl is zero, $\nabla \cdot (\nabla^2 \mathbf{u}) = -\nabla \cdot (\nabla \times \boldsymbol{\omega}) = 0$. By simplifying the aforementioned assumptions and rearranging the terms, we have

$$\nabla^2 P = -\nabla^2 k + \nabla \cdot (\mathbf{u} \times \boldsymbol{\omega}). \tag{4}$$

By writing each term of Eq. (4) in its partial differential form, we obtain

$$\nabla^2 P = \frac{\partial^2 P}{\partial x^2} + \frac{\partial^2 P}{\partial y^2} + \frac{\partial^2 P}{\partial z^2}, \tag{5}$$

$$\nabla^2 k = \frac{1}{2}\frac{\partial^2 u_x^2}{\partial x^2} + \frac{1}{2}\frac{\partial^2 u_y^2}{\partial y^2} + \frac{1}{2}\frac{\partial^2 u_z^2}{\partial z^2}, \tag{6}$$

$$\nabla \cdot (\mathbf{u} \times \boldsymbol{\omega}) = \frac{\partial \left[u_y \left(\frac{\partial u_y}{\partial x} - \frac{\partial u_x}{\partial y} \right) - u_z \left(\frac{\partial u_x}{\partial z} - \frac{\partial u_z}{\partial x} \right) \right]}{\partial x}$$
$$- \frac{\partial \left[u_x \left(\frac{\partial u_y}{\partial x} - \frac{\partial u_x}{\partial y} \right) - u_z \left(\frac{\partial u_z}{\partial y} - \frac{\partial u_y}{\partial z} \right) \right]}{\partial y}$$
$$+ \frac{\partial \left[u_x \left(\frac{\partial u_x}{\partial z} - \frac{\partial u_z}{\partial x} \right) - u_y \left(\frac{\partial u_z}{\partial y} - \frac{\partial u_y}{\partial z} \right) \right]}{\partial z}. \tag{7}$$

By considering a two-dimensional flow, the terms related to the z direction vanish, and the equation can be written as

$$\frac{\partial^2 P}{\partial x^2} + \frac{\partial^2 P}{\partial y^2} = \frac{1}{2}\frac{\partial^2 u_x^2}{\partial x^2} + \frac{1}{2}\frac{\partial^2 u_y^2}{\partial y^2}$$
$$+ \frac{\partial \left[u_y \left(\frac{\partial u_y}{\partial x} - \frac{\partial u_x}{\partial y} \right) \right]}{\partial x} - \frac{\partial \left[u_x \left(\frac{\partial u_y}{\partial x} - \frac{\partial u_x}{\partial y} \right) \right]}{\partial y}. \tag{8}$$

The simplifying assumptions applied to the Navier-Stokes equations Eq. (1), are of *i.* stationary, *ii.* incompressible, *iii.* two-dimensional flow. Thus, by applying the aforementioned hypotheses in the Navier-Stokes equations and by taking the divergence of the remaining terms, we find the Poisson relation shown in Eq. (8). It's worth noting that disregarding the terms related to the z direction leads to an overestimation of the pressure. When the vortex structure is stretched due to the upward movement of the diverging disk, the cross-section of the vortex shrinks. Consequently, the angular momentum conservation dictates that the rotation rate must increase, resulting in a decrease in pressure inside the vortex core.

2.3. Poisson solver

The terms related to the laplacian of the kinetic energy, Eq. (6), are determined using the second-order centered difference approximation of the second derivative due to its more accurate approximation (Nocedal & Wright, 2006). The vorticity on Eq. (7) is estimated by the 'circulation' method (Adrian & Westerweel, 2011). Then, the divergence of the cross product between the velocity vector and the vorticity vector is estimated using the second-order centered difference approximation of the first derivative.

Eq. (8) can be re-written as $\nabla^2 P - S = 0$, which represents a Poisson equation, where $S = -\nabla^2 k + \nabla \cdot (\mathbf{u} \times \boldsymbol{\omega})$, where these terms are related to the velocity vector. To numerically solve the Poisson equation, the successive over-relaxation (SOR) method is applied, which speeds up the convergence. The recommended value of the SOR convergence factor β is about 1.7 (White, 2009). The grid size Δ is the vector spacing, which is of 0.4 mm in both directions. The numerical formulation of the Poisson solver is therefore as follows

$$P_{i,j} = P_{i,j} + \frac{\beta}{4}(P_{i,j+1} + P_{i,j-1} + P_{i+1,j} + P_{i-1,j} - 4P_{i,j} - \Delta^2 S_{i,j}). \tag{9}$$

In order to numerically solve the Poisson relation for the present study, the Bernoulli equation at the boundary conditions is applied, and 140,000 iterations are necessary to achieve convergence.
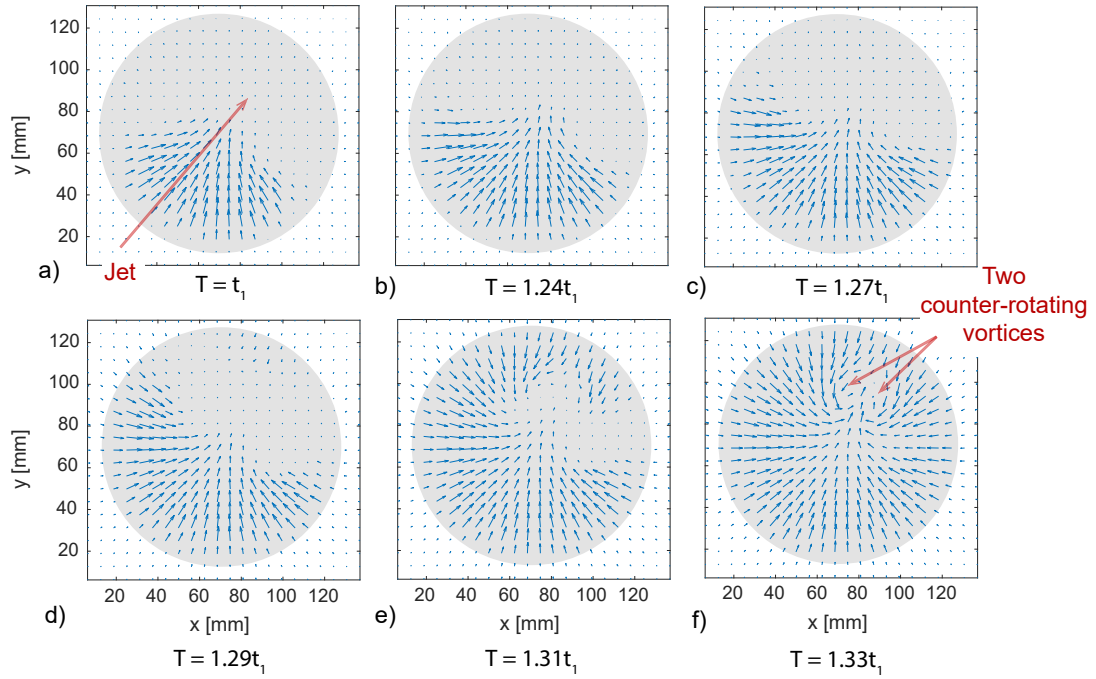
3. Results

3.1. The formation of the two counter-rotating vortices

The flow developing in the thin film between the disks is investigated with planar PIV, where the measurement plane is at 2.7 mm distance from the bottom disk. Its time evolution is presented in Figure 2. The gray circles depict the positions of the disks, while the blue arrows indicate the instantaneous 2D velocity vector field. The first frame, which is taken at approximately 63.1 ms after the separation of the two disks and is presented in Figure 2a, shows that the small angle between the two disks triggers the generation of a strong entry jet. This is tagged with a red arrow. The formation of the two counter-rotating vortices (Figure 2f) occurs following the entry of the non-uniform radial jet flow. The development of this non-uniform jet flow is illustrated from Figure 2b to Figure 2e at time intervals of approximately 1.57 ms.

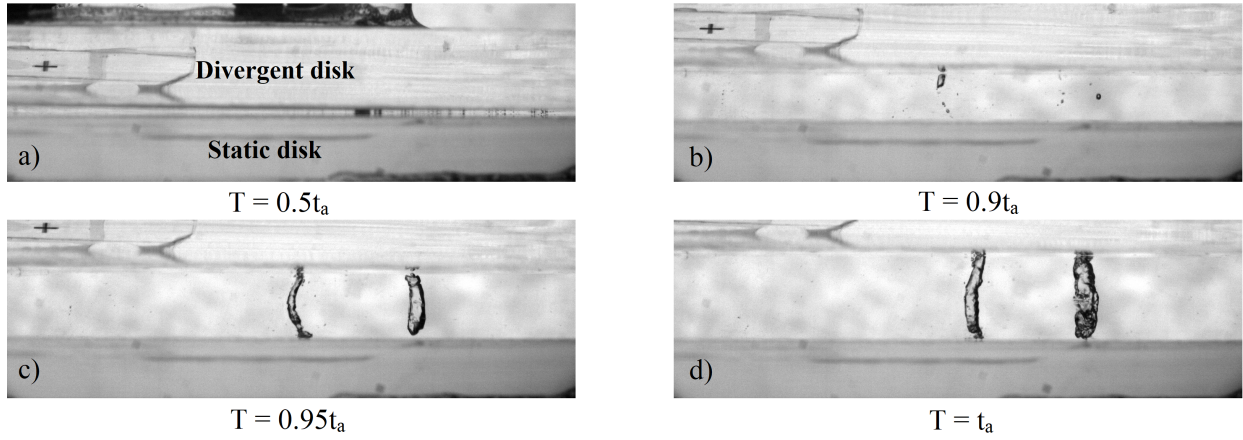### 3.2. Analysis of the studied cases

In Figure 3, shadowgraphy images are presented for Case 1 at three different time instants preceding the point of maximum acceleration and at the point of maximum acceleration (t_a) itself.

Figure 2. Formation of the two counter-rotating vortices due to non-uniform flow in the radial direction (jet). The laser sheet is aligned parallel to the disks, and is located about 2.7 mm above the bottom disk. The case displayed here to illustrate the generation of the vortices is a non-cavitating one.

Bubbles having a diameter of approximately 0.15 mm can be observed in the gap between the two disks, immediately after the top disk detaches from the bottom one (see Figure 3a). They possibly originate from small crevices in the surface of the disks (Franc & Michel, 2005). The observed bubbles exhibit a spiraling motion inside the two vortices before being trapped inside their cores (see Figure 3b) (Kelly et al., 2021). The appearance of bubbles in this phase is a shared feature between Case 1 and Case 2. When moving from $0.9t_a$ to $0.95t_a$, therefore almost at the instant of maximum acceleration, stable vortex cavities begin to appear (see Figure 3b and 3c). The size of the two vortex cavities increases when the top disk reaches the maximum acceleration. In Case 1, the bubbles trapped inside the left vortex gradually grow in size until they form the observed cavity, whereas the bubbles trapped inside the right vortex do not vary importantly in size, and the onset of the stable cavity occurs abruptly. From observation of the corresponding shadowgraphy images, Case 2 does not exhibit any vortex cavities, but tiny bubbles following a cylindrical path can be seen in each of the two vortex cores.

The vortex cavities associated to Case 1 can either be produced by the coalescence of free non-condensable gas in the form of bubbles or be the result of a cavitation process. A first evidence that cavitation could be the reason behind the appearance of the vortex cavities is that they appear for an acceleration of the diverging disk of 93 m s^{-2}, i.e. for Case 1, but they do not appear for an acceleration of 28 m s^{-2}, for case Case 2. This is because the circulation produced by the vortices in the latter case may not be sufficiently large to induce a pressure drop in the cores of the vortices,
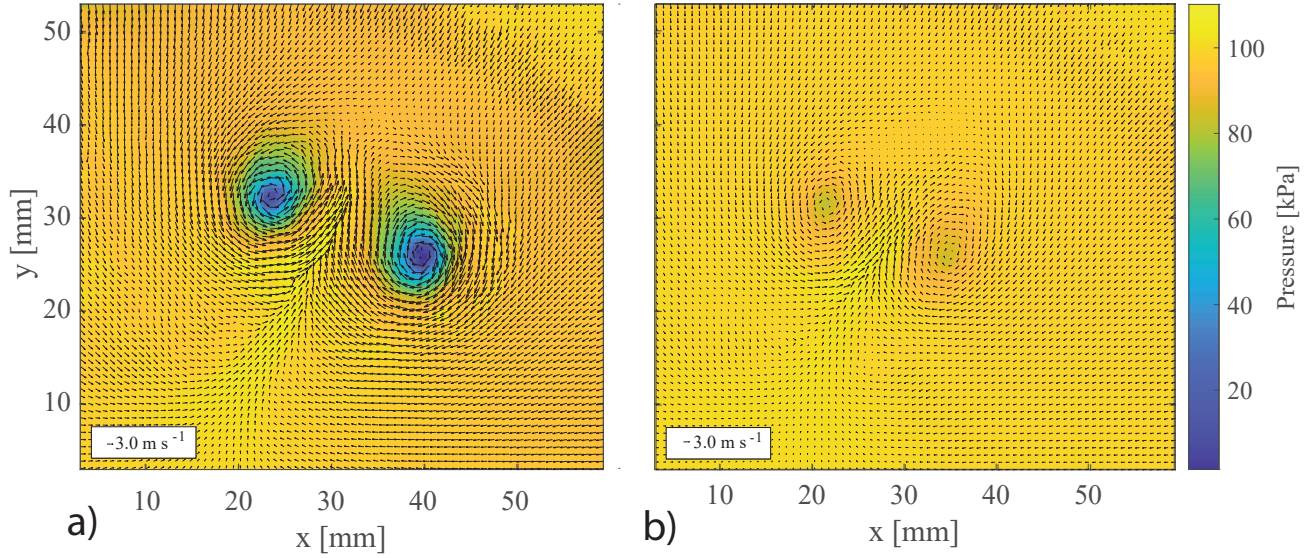
Figure 3. Shadowgraphy images at different time instants and viewed from a vertical plane showing the formation of two vortex cavities for Case 1. Here, t_a is the time needed to the top diverging disk to reach the maximum acceleration.

such to have locally a pressure lower than the vapor pressure. The second indication is the cavitation rebound that occurs during the collapse of cavitating vortices, characterized by the Besant problem (Besant, 1859).
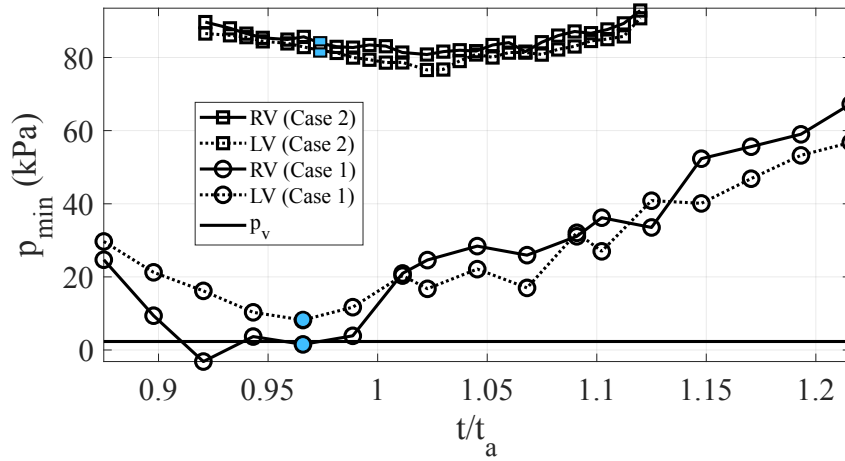
3.3. PIV data and Pressure Reconstruction

To give further support to the hypothesis that the origin of the observed bubbles is cavitation, the pressure field is reconstructed from PIV data in the region where the vortices occur. Simplifying assumptions to the Navier-Stokes equations are introduced, and a Poisson solver is applied. The estimated pressure fields for the two cases are presented in Figure 3, where the velocity vector field is also depicted. It is important to mention that the velocity field shown in Figure 3 is obtained from the image oversampling of ten repetitions (Samarage et al., 2012). The absolute pressure in the core of the right vortex in Figure 3a is 1.53 kPa, i.e., lower than the vapour pressure, with the latter being 2.33 kPa for the experimental conditions. This represents an additional important indication that a phase transition occurs at the core of the vortices in Case 1. In Figure 3b, where the velocity field and pressure distribution for Case 2 are presented, the pressure inside the vortex is 81.9kPa for the left vortex and 78.2kPa for the right vortex, therefore much larger than the vapour pressure.

Figure 4. Velocity vector fields as reconstructed from PIV and sum of correlation, and pressure fields obtained from the velocity data for Case 1 in a), and Case 2 in b). Velocity and pressure fields obtained at T=0.95t_a, as in the shadowgraphy image of Figure 2c.

By performing correlation averaging and applying a Poisson solver for different instants for the non-cavitating and cavitating cases, a graph of the lowest pressure value inside the vortex cores, p_{min}, as a function of time can be plotted (Figure 5). The time development of the vortices and their onset to cavitation, which we have thus far illustrated from shadowgraphy images for Case 1 (Figure 3), can here be interpreted in relation to the variation of the minimum pressure inside the cores of the vortices. The lowest value of pressure for Case 1 in the core of the left vortex is 8.2 kPa, i.e., mildly larger than the vapour pressure. This could be attributed either to the correlation averaging from different vertical positions of the disk, or to the simplifying assumptions in the estimate of the pressure field, or to the PIV spatial resolution.

Figure 5. Time evolution of lowest pressure in the core, p_{min}, of the two vortices, as a function of the non-dimensionalized time, where t_a, the time of maximum acceleration, has been used for non-dimensionalization. Blue-filled symbols represent the value of the lowest pressure for the instant shown in Figure 4, at the time instant of approximately $0.97t_a$.
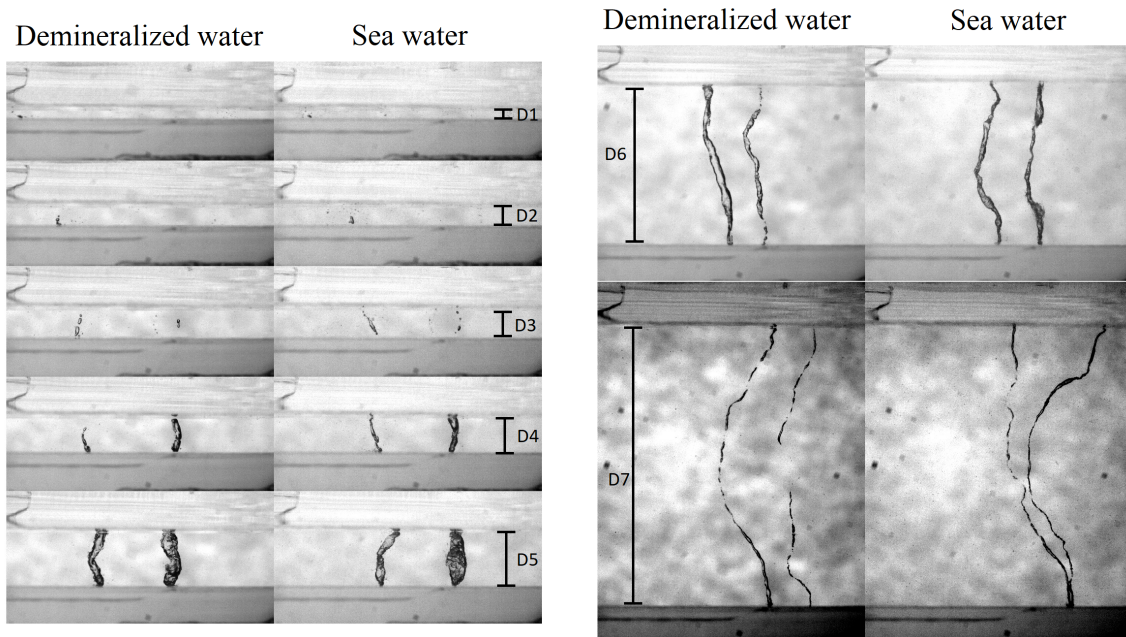
The observation obtained from shadowgraphy, i.e. that the onset of cavitation is abrupt for the right vortex if compared to the left one, can here be explained by the relatively lower values of pressure of the right vortex (Figure 5). Consistently, the left cavitating vortex always forms more slowly than the right one.

3.4. Water Quality

Shadowgraphy recordings were performed both in demineralized water and sea water. The sea water is made by adding 1.153 kg of Instant Ocean® synthetic sea salt to the tank filled with 33 liters of demineralized water, in such a way to obtain a salinity of 35 parts per thousand. This sea salt was used by Winkel et al. (2004) to assess the effect of water quality on bubble-size distributions produced by wall injection of air into a flow. In addition, the dissolved oxygen (DO) content for the saltwater is $7.66\,\text{mg L}^{-1} \pm 0.024\,\text{mg L}^{-1}$ (104.75 %a.s. $\pm$ 0.44 %a.s.), whereas for the demineralized water is $8.68\,\text{mg L}^{-1} \pm 0.031\,\text{mg L}^{-1}$ (99.43 %a.s. $\pm$ 0.18 %a.s.)

In Figure 6, we can see the comparison between shadowgraphy recordings of demineralized water and sea water for the cavitating case (Case 1). In order to see the inception, development, and collapse of the cavitating vortices, shadography recordings for different instants of upward movement of the diverging disk are shown. In distance D1, it is possible to see the bubble responsible for the inception of the left cavitating vortex. Once this bubble undergoes the lower pressure region between the disk gap, onset cavitation occurs; see recordings for distances D2 and D3. In the distance range between D4 and D5, the cavitating vortices are formed and grow in diameter. Due to the movement of the diverging disk, the vortices are stretched, reducing the diameter size
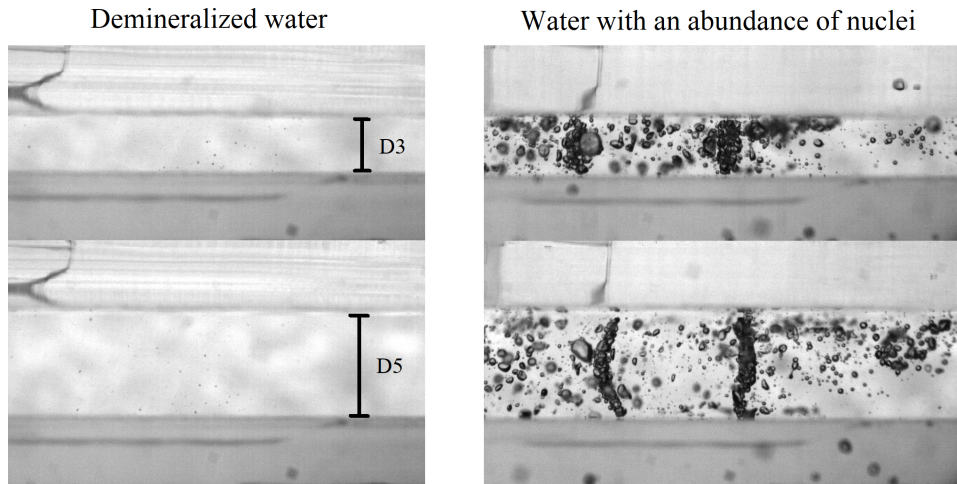
Figure 6. Shadowgraphy comparison between demineralized water and sea water for the cavitating case. The distance between the two disks are approximately: D1 = 1.8 mm, D2 = 3.3 mm, D3 = 5 mm, D4 = 6.1 mm, D5 = 9.3 mm, D6 = 27.7 mm, D7 = 50 mm.

shown in D6. When the diverging disk reaches its final position, the vortices collapse, see D7. In conclusion, no difference was noticed in the inception, development, and collapse of the cavitating vortices by the shadowgraphy recordings after changing the water from demineralized to sea water.

The effect on cavitation of water with an abundance of nuclei is also investigated, using a commercially available sparkling water for this purpose. The dissolved oxygen content was also measured for this case, yielding results of 0.84 mg L^{-1} ± 0.44 mg L^{-1} (9.18 %a.s. ± 4.87 %a.s.). These average DO values are lower compared to demineralized water and sea water because the sparkling water is supersaturated with carbon dioxide. However, the standard deviation is higher in this case due to the rapid dissipation of the bubbles, leading to more significant variations in the oxygen content measurements.

In Figure 7, the left panel shows shadowgraphy image of the non-cavitating case (Case 2) using demineralized water, while the right panel presents a shadowgraphy image for the same case, but now the water contains an abundance of nuclei. For both panels, two different time instants are shown on top of each other, characterized by a separation of the disks of D3 and D5 respectively for the top frame and the bottom frame. In the right panel, it can be observed that the large content of bubbles leads to the formation of two cavities. These are most probably pseudo-cavities (Atlar et al., 2002) resulting from the coalescence of the free non-condensable gases contained in the sparkling water, as they tend to move into the low-pressure regions produced by the cores of

Demineralized water   Water with an abundance of nuclei

Figure 7. Shadowgraphy comparison between demineralized water and water with an abundance of nuclei for the non-cavitating case. The distance between the two disks are approximately: D3 = 5mm and D5 = 9.3mm.

the vortices.

According to Liu et al. (2023) among others, salt affects the size and quantity of bubbles due to the inhibition of bubble coalescence. From our experiments, dissolving salt in the water when the water is depleted of nuclei produces negligible effects on cavitation. On the other hand, an abundance of nuclei profoundly affects cavitation, as observed recently by Venning et al. (2022) among others. In lieu of these observations, we hypothesise that modifying the chemical composition of water by adding salt (or surfactants) could produce important effects only if the water is rich in nuclei. This hypothesis will be assessed in the near future by performing these experiments using fresh water as well as salt water in presence of an abundance of nuclei.

4. Conclusions

In this work, the flow at the interface of two diverging disks, the so-called negative squeeze film, is studied with shadowgraphy and PIV. The acceleration of the top disk determines a depressurization of the gap, which generates a strong non-uniform jet flow. This is associated to the formation of two counter-rotating vortices, at the cores of which cavities are observed from high-speed shadowgraphy. Evidence that these cavities result from a cavitation process and do not form by coalescence of free non-condensable gas is gained by the reconstruction of the pressure field from velocity data. No evidence of chemical water quality effect on cavitation dynamics is found by comparing the shadowgraphy recordings for fresh water and sea water for the cavitating case. However, for water with an abundance of nuclei, pseudo-cavities form for the non-cavitating case.

Acknowledgements

References

Adrian, R., & Westerweel, J. (2011). *Particle Image Velocimetry*. United Kingdom: Cambridge University Press.

Atlar, M., Billet, M., Briançon-Marjollet, L., Ceccio, S., Kim, Y.-G., Oshima, A., & Song, I.-H. (2002, September). The Specialist Committee on Water Quality and Cavitation. *: Proceedings of the 23rd International Towing Tank Conference,, II*.

Besant, W. H. (1859). *A Treatise On Hydrostatics and Hydrodynamics*. Palala Press. (original-date: 1859)

Brandner, P. A., Venning, J. A., & Pearce, B. W. (2022). Nucleation effects on cavitation about a sphere. *J. Fluid Mech.*, *946*, A1.

Erinin, M. A., Néel, B., Mazzatenta, M. T., Duncan, J. H., & Deike, L. (2023, May). Comparison between shadow imaging and in-line holography for measuring droplet size distributions. *Experiments in Fluids*, *64*(5), 96. Retrieved 2024-01-05, from `https://link.springer.com/10.1007/s00348-023-03633-8` doi: 10.1007/s00348-023-03633-8

Franc, J.-P., & Michel, J.-M. (2005). *Fundamentals of Cavitation* (Vol. 76; R. Moreau, Ed.). Dordrecht: Springer Netherlands. Retrieved 2024-02-08, from `https://link.springer.com/10.1007/1-4020-2233-6` doi: 10.1007/1-4020-2233-6

Kawchuk, G. N., Fryer, J., Jaremko, J. L., Zeng, H., Rowe, L., & Thompson, R. (2015, April). Real-Time Visualization of Joint Cavitation. *PLOS ONE*, *10*(4), e0119470. Retrieved 2024-03-04, from `https://dx.plos.org/10.1371/journal.pone.0119470` doi: 10.1371/journal.pone.0119470

Kelly, R., Goldstein, D. B., Suryanarayanan, S., Botto Tornielli, M., & Handler, R. A. (2021, June). The nature of bubble entrapment in a Lamb–Oseen vortex. *Physics of Fluids*, *33*(6), 061702. Retrieved 2024-02-12, from `https://pubs.aip.org/pof/article/33/6/061702/1015596/The-nature-of-bubble-entrapment-in-a-Lamb-Oseen` doi: 10.1063/5.0053658

Khoo, M. T., Venning, J. A., Pearce, B. W., & Brandner, P. A. (2021, October). Nucleation and cavitation number effects on tip vortex cavitation dynamics and noise. *Experiments in Fluids*, *62*(10), 216. Retrieved 2024-03-04, from `https://link.springer.com/10.1007/s00348-021-03308-2` doi: 10.1007/s00348-021-03308-2

Konrath, R., & Schröder, W. (2002, November). Telecentric lenses for imaging in particle image velocimetry: a new stereoscopic approach. *Experiments in Fluids*, *33*(5), 703–708. Retrieved 2024-01-05, from `http://link.springer.com/10.1007/s00348-002-0531-7` doi: 10.1007/s00348-002-0531-7

Liu, B., Manica, R., Liu, Q., Xu, Z., Klaseboer, E., & Yang, Q. (2023, September). Nanoscale Transport during Liquid Film Thinning Inhibits Bubble Coalescing Behavior in Electrolyte Solutions. *Physical Review Letters*, *131*(10), 104003. Retrieved 2024-06-20, from `https://link.aps.org/doi/10.1103/PhysRevLett.131.104003` doi: 10.1103/PhysRevLett.131.104003

Meinhart, C. D., Wereley, S. T., & Santiago, J. G. (2000, June). A PIV Algorithm for Estimating Time-Averaged Velocity Fields. *Journal of Fluids Engineering*, *122*(2), 285–289. Retrieved 2024-01-05, from `https://asmedigitalcollection.asme.org/fluidsengineering/article/122/2/285/459651/A-PIV-Algorithm-for-Estimating-TimeAveraged` doi: 10.1115/1.483256

Nanda, S., Westerweel, J., Van Terwisga, T., & Elsinga, G. (2022, November). Mechanisms for diffusion-driven growth of cavitating wing-tip vortices. *International Journal of Multiphase Flow*, *156*, 104146. Retrieved 2024-01-12, from `https://linkinghub.elsevier.com/retrieve/pii/S0301932222001380` doi: 10.1016/j.ijmultiphaseflow.2022.104146

Nocedal, J., & Wright, S. J. (2006). *Numerical Optimization* (2e ed.). New York, NY, USA: Springer.

Resch, M., & Scheidl, R. (2014, June). A model for fluid stiction of quickly separating circular plates. *Proceedings of the Institution of Mechanical Engineers, Part C: Journal of Mechanical Engineering Science*, *228*(9), 1540–1556. Retrieved 2024-03-04, from `http://journals.sagepub.com/doi/10.1177/0954406213509613` doi: 10.1177/0954406213509613

Reynolds, O. (1886, December). IV. On the theory of lubrication and its application to Mr. Beauchamp tower's experiments, including an experimental determination of the viscosity of olive oil. *Philosophical Transactions of the Royal Society of London*, *177*, 157–234. Retrieved 2024-01-05, from `https://royalsocietypublishing.org/doi/10.1098/rstl.1886.0005` doi: 10.1098/rstl.1886.0005

Samarage, C. R., Carberry, J., Hourigan, K., & Fouras, A. (2012, March). Optimisation of temporal averaging processes in PIV. *Experiments in Fluids*, *52*(3), 617–631. Retrieved 2024-01-09, from

`http://link.springer.com/10.1007/s00348-011-1080-8` doi: 10.1007/s00348-011
-1080-8

Venning, J. A., Pearce, B. W., & Brandner, P. A. (2022, September). Nucleation effects on cloud cavitation about a hydrofoil. *Journal of Fluid Mechanics*, *947*, A1. Retrieved 2024-01-04, from `https://www.cambridge.org/core/product/identifier/S0022112022005353/type/journal_article` doi: 10.1017/jfm.2022.535

White, F. M. (2009). *Fluid mechanics* (6th ed ed.). New York, NY: McGraw-Hill.

Winkel, E. S., Ceccio, S. L., Dowling, D. R., & Perlin, M. (2004, December). Bubble-size distributions produced by wall injection of air into flowing freshwater, saltwater and surfactant solutions. *Experiments in Fluids*, *37*(6), 802–810. Retrieved 2024-01-05, from `http://link.springer.com/10.1007/s00348-004-0850-y` doi: 10.1007/s00348-004-0850-y